JOURNAL OF AIRCRAFT
Vol. 34, No. 1, January–February 1997

Forward-Flight Analysis of Slatted Rotors Using Navier–Stokes Methods

A. Bangalore* and L. N. Sankar†
Georgia Institute of Technology, Atlanta, Georgia 30332

The objective of this study is to evaluate the aerodynamic effects of leading-edge slats on rotor blades under high-speed forward-flight conditions. A partial-span leading-edge slat is proposed for the inboard portion of the existing UH-60A rotor. Some two-dimensional slat studies are done to optimize the slat orientation at low subsonic Mach numbers. A multizone unsteady three-dimensional compressible Navier–Stokes solver is developed to compute such rotor/slat configurations. The rotor wake is captured from first principles. Some forward-flight results are presented for the UH-60A slatted rotor and compared with the baseline rotor case. The surface pressures and the force coefficients indicate that the slat is beneficial in reducing the retreating side dynamic stall. It was found that the slat reduces the torque and pitching moments on the retreating side compared to the baseline configuration.

Introduction

NEXT-GENERATION combat helicopters are expected to have high maneuverability, agility, and good handling qualities. Highly maneuverable rotorcraft are particularly desirable in deep-penetration operations, air-to-air combat situations, and nap-of-the-Earth operations. The first step for achieving higher maneuverability is to improve the aerodynamic performance of the main rotor, and in particular, to increase the maximum thrust generated by the rotor and reduce or eliminate the retreating blade stall.

During the late 1970s, rotorcraft airfoil sections were designed to achieve high maximum lift coefficients $C_{l\max}$, and low zero-lift drag coefficients C_{d0}.[1–3] Rotorcraft airfoils such as Hughes HH-02, Vertol VR-7, VR-12, and Sikorsky SC-1095 have shown significantly higher $C_{l\max}$ and lower C_{d0}[4] and good high-speed characteristics. However, the U.S. Army's future needs require significant improvement in lift above the level of the current airfoils. Further dramatic improvement in airfoil lift capability without considerable compromises in pitching moment or drag divergence characteristics may be unrealistic for conventional airfoils.[5] An increase in the blade area of the present-day single-element rotors causes an increase in the blade weight and may decrease the useful payload. An increase in the camber of the airfoils results in undesirable drag divergence characteristics and higher pitching moment levels leading to higher control loads. Highly cambered single-element airfoils also have poor dynamic stall characteristics that lead to structural vibration problems. The rotor blade with a leading-edge slat is expected to achieve higher thrust levels compared to a single-element airfoil without much increase in blade weight.[6]

McAlister et al.[4] have experimentally studied the dynamic stall characteristics of a Boeing vertol airfoil with and without slat, and demonstrated that the deployment of the slat shrinks the hysteresis loop and increases the average lift levels during the oscillation cycle. Noonan et al.[5] conducted experiments to study the aerodynamic performance characteristics of a slotted rotorcraft airfoil. Their studies indicate that the use of a slotted airfoil leads to significant improvements in $C_{l\max}$ with minimum adverse impact on drag and pitching moment characteristics. Yu et al.[6] have presented the potential of improving the lift, drag, and moment characteristics of airfoil sections on rotor blades with high-lift devices such as slats, deformable leading edges, and upper-surface blowing. Recently, the present authors[7] studied two rotor configurations (VR7 and UH-60A) with leading-edge slats in hover using the three-dimensional unsteady compressible Navier–Stokes equations. In the case of the VR7 rotor blade, a full-span leading-edge slat was employed and it was shown that at high collective pitch settings the blade stall angle was increased, leading to higher thrust and reduced torque. A partial span slat was used in the case of the UH-60A rotor blade and at moderate collective pitch angles the slat was seen to improve the hover performance of the baseline rotor.

Benefits of Slatted Rotors

The primary benefit of a leading-edge slat on a rotor blade is to improve the aerodynamic performance of the rotor in hover and forward-flight conditions. The maximum thrust generated by the rotor in hover is limited by blade stall. High-lift devices such as leading-edge slats delay blade stall and increase the maximum thrust generated by the rotor. Thus, an increase in useful payload in hover and climb can be realized. The leading-edge slat does not add a significant amount of blade weight, particularly if the slats are deployed permanently to reduce the complexity of the actuators and active control devices.

In high-speed forward-flight situations, the maximum thrust on the retreating blade falls because of the decrease in dynamic pressure and also the occurrence of dynamic stall because of the changes in blade pitch. The thrust achievable is thus limited throughout the forward-speed range. Maximum thrust possible on the advancing side increases, but is unrealizable because of the retreating blade restriction. As the advancing blade tip Mach number approaches unity, the lift generated is restricted by shock-induced flow separation. Drag divergence and pitching moment divergence also limit the maximum speed achievable. Thus, the envelope is bounded by a limit on thrust from retreating blade stall and a limit on forward speed from advancing blade compressibility effects.[8] Also, retreating blade stall leads to large, highly unsteady pitching moments. These pitching moment variations lead to high control loads and vibration levels. The blade torsional moments may also increase, and in some cases, lead to stall flutter.

Received Feb. 11, 1996; revision received Sept. 3, 1996; accepted for publication Nov. 12, 1996.

*Graduate Research Assistant, School of Aerospace Engineering; currently Research Scientist, Flow Analysis Inc., Brooklyn, NY 11209. Member AIAA.

†Professor, School of Aerospace Engineering. Senior Member AIAA.

Based on the two-dimensional studies,[5–7] and also the three-dimensional hover calculations,[7] it may be expected that a leading-edge slat will reduce or eliminate the dynamic stall on the retreating side. Thus, the thrust limit imposed by the blade stall could be increased by using a slat. The sectional drag levels may also be reduced on the retreating side, lowering the torque. The slat also reduces the pitching moment oscillations caused by the dynamic stall and reduces the pitch link loads and vibration levels. These beneficial effects of a slat must, of course, be weighted against any adverse effects on the advancing side. To date, such a comprehensive study has not been done.

Numerical Features

The three-dimensional unsteady compressible Reynolds-averaged Navier–Stokes equations are solved numerically using a time-marching scheme. A hybrid alternating direction implicit (ADI) scheme[9] is used in the present work. The inviscid flux derivatives are calculated using a third-order Roe upwind scheme,[10] based on a finite volume approach. The viscous derivatives are calculated using a second-order standard central difference scheme. The Baldwin–Lomax algebraic turbulence model[11] is used in the present calculations. The formulation of the hybrid-implicit scheme, boundary conditions, and the multizone methodology are described in detail.[12] The hybrid-implicit scheme has been validated for a number of fixed-wing and rotary-wing configurations, both in steady and unsteady flight conditions.[9,12,13]

Results and Discussion

Computational Grid

Figure 1 shows a typical three-zone H-grid around a slatted airfoil. As shown in Fig. 1, there are three zones in the normal direction for a two-component airfoil. The far-field boundaries are at a distance of six chord lengths from the body surface. A typical two-component airfoil grid consists of 120 points in the streamwise direction, 40 points in the normal direction in the top and bottom zones, and 30 points in the middle zone. This type of multizone H-grid was successfully used in computing flow over a five-component Boeing 737 airfoil[14] in a previous study.

The forward-flight calculations for a four-bladed single/multielement rotor are done using H–O type grids around each rotor blade. An H–O type grid is generated around each blade and connected at the zonal interfaces. The top view of all the blade grids at a particular azimuth location is shown in Fig. 2. At each time step, each blade grid is rotated in pitch within the flow solver and also in the azimuthal direction. The flow solver ensures that the zonal interfaces connecting any two adjacent blade grids are patched with a point-to-point overlap.

SC1095 Slat Studies

The objective of the present work is to evaluate the use of a high-lift device such as a leading-edge slat for a highly twisted realistic rotor (UH-60A) blade. The design of a slat section for the existing SC1095 airfoil for a range of Mach numbers and Reynolds numbers involves an elaborate analysis of the high-lift airfoil with different slat shapes and orientations. A detailed three-dimensional optimization study is desirable, but is not feasible because of the enormous amount of computer resources required. As a first step, the SC1095/slat configuration was analyzed in the two-dimensional mode with a fixed slat shape at two different slat orientations and low subsonic Mach numbers.

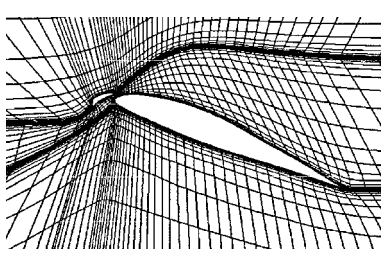

Fig. 1 Two-dimensional multizone H-grid.

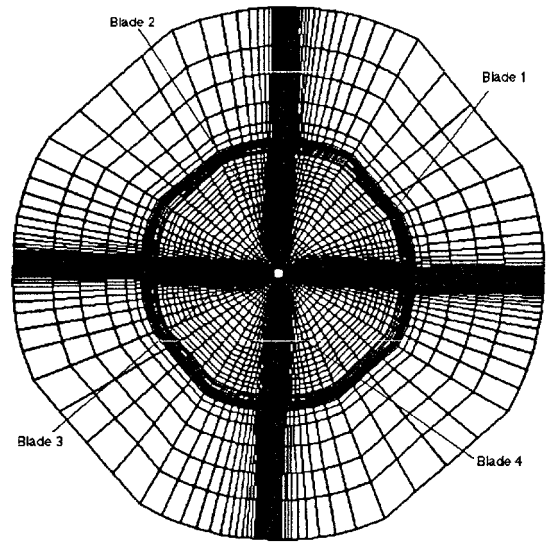

Fig. 2 Top view of a four-bladed multizone H–O grid in forward flight.

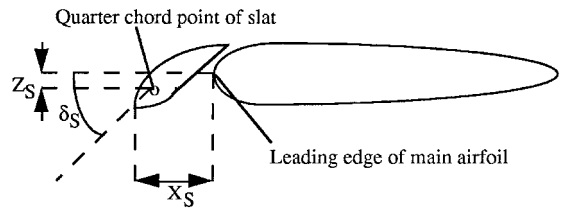

Fig. 3 Schematic of SC-1095 slatted airfoil (not to scale).

The airfoil profile of the slat is identical to the shape of the main airfoil, with a reduced chord and thickness distribution. The chord length of the slat is 10% that of the main airfoil. As shown in Fig. 3, X_S is the distance of the quarter-chord point of the slat from the leading edge of the main airfoil normalized with respect to the main chord, Z_S is the vertical shift in the quarter-chord point of the slat from the leading-edge point of the main airfoil, and δ_S is the angle of rotation of the slat pivoted at the quarter-chord point and is measured in the anticlockwise direction.

The slatted SC1095 airfoil is analyzed using the multizone Navier–Stokes solver at two subsonic Mach numbers of 0.2 and 0.38 at a Reynolds number of 2.2×10^6. Figure 4 shows the sectional lift and drag coefficients of baseline and slatted sections of SC1095 airfoil plotted against angle of attack for a Mach number of 0.38. Two slat angles δ_S (25 and 34 deg), as defined in Fig. 3, are selected for comparison purposes. In both the cases, the parameters X_S and Z_S are $0.06c$ and $0.008c$, respectively.

Figure 4 shows that at both slat orientations the stall angle is increased. There is an increase in the lift values and a decrease in the drag coefficients at higher angles of attack when compared to the baseline values. At lower angles of attack below 8 deg, the drag coefficients of the slatted airfoils are higher than the baseline values because of a mild separation on the lower surface of the slat. As the angle of attack is increased, the flow through the gap between the slat and the main element energizes the flow on the upper surface of the main airfoil, thus delaying stall. Also, it is seen that as the slat angle is increased from 25 to 34 deg in the anticlockwise di-

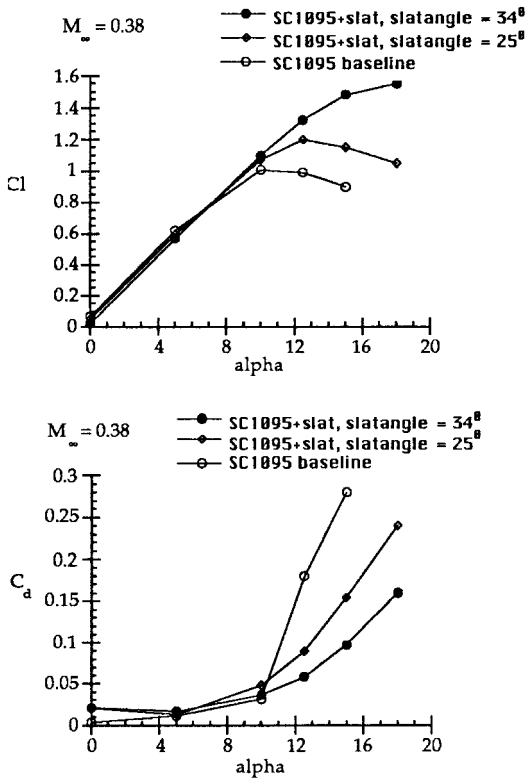

Fig. 4 Lift and drag coefficients vs alpha, baseline, and slatted SC-1095 airfoils, $M_\infty = 0.38$, $Re = 2.2 \times 10^6$.

rection, the percentage of lift increases with respect to the baseline airfoil increases, and a higher percentage of reduction in drag coefficients is observed at higher angles of attack. To obtain a true optimum slat geometry for a desired range of Mach numbers and angles of attack, a parametric study needs to be done by varying the slat shape, horizontal and vertical distances X_S and Z_S, and the slat angle δ_S.

From the previous two-dimensional analysis, the benefits of the proposed slat for the SC1095 airfoil was confirmed. This slat section with a δ_S = 34-deg orientation was then incorporated into the three-dimensional UH-60A rotor blade.

UH-60A Baseline Rotor

The schematic of the model UH-60A rotor blade geometry is shown in Fig. 5. The flow condition simulated in this calculation is high-speed forward-flight with an advance ratio μ of 0.3 and a tip Mach number of 0.628. The model rotor was trimmed to zero first harmonic flapping in the experiments.[15] The geometric pitch time history is taken out of Lorber's[15] data. This pitch distribution includes the built-in structural twist distribution, cyclic and collective pitch, and torsional deflections around the azimuth. The collective pitch is 8.8 deg. These pitch data are converted in to a table of sectional angle-of-attack (minus the inflow) values at all of the azimuthal and spanwise locations. At each time step of the solution process, different spanwise sections of the rotor blade are rotated in pitch according to the tabular data.

The computational grid used in this calculation consists of four H–O blade grids. Each block spans a quarter of the azimuth (i.e., 90 deg) and the adjacent blocks are patched with a point-to-point overlap at the zonal interfaces. Each blade grid consists of 90 points in the azimuthal direction, 43 points in the spanwise direction, and 80 points in the normal direction. At each time step, the blade grids rotate in the azimuthal direction and also rotate in pitch according to the pitch distribution.[15] Ahmad et al.[16,17] have performed forward-flight calculations for two- and four-bladed rotor systems using moving overset grids with user-specified blade motions. In the present method, the zonal interfaces have a point-to-point overlap. The zonal interfaces remain aligned at each time step, even though the interior of the grid rotates with different pitch amplitudes. The time step Δt taken in the present calculation is 0.01, which corresponds to an azimuth of 0.023 deg for the chosen tip Mach number.

Figure 6 shows the surface pressures plotted in the first quadrant (ψ = 0 and 30 deg) at 77.5 and 94.5%R radial locations. The pressure values are nondimensionalized with respect

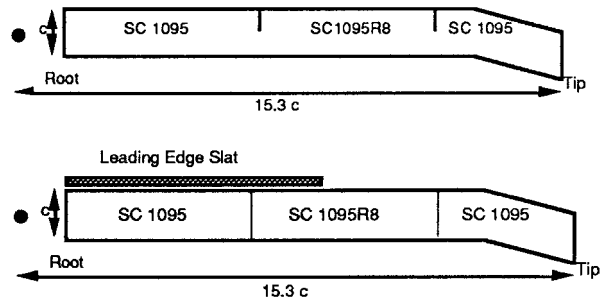

Fig. 5 Schematic of baseline and slatted UH-60A rotor blades.

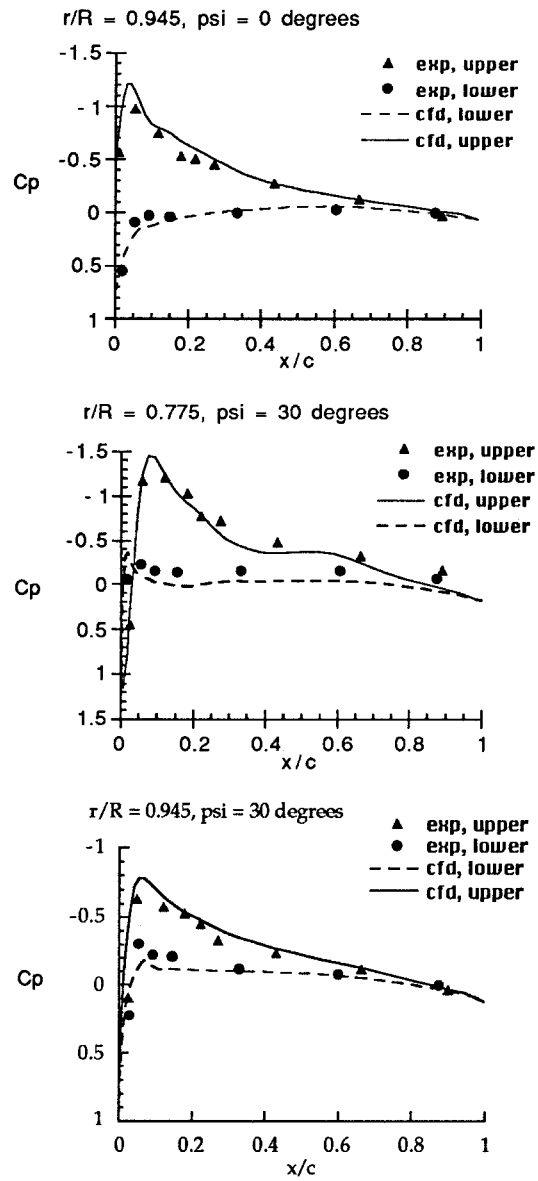

Fig. 6 Surface pressure distribution, first quadrant, $M_{tip} = 0.628$, advance ratio = 0.3, UH-60A baseline rotor.

to the local dynamic pressure. Figure 7 shows the surface pressures in the second quadrant (ψ = 90–120 deg). The tip region experiences negative loads in the second quadrant at ψ = 120 deg. At ψ = 100 deg a shock is formed on the lower surface near the tip region as a result of the negative pitch distribution. The computed pressures match well in the regions where the flow is smooth with no discontinuities.

The retreating side surface pressures at 40% radial location and ψ = 220, 270, and 320 deg are shown in Fig. 8. The leading-edge peak is largely underpredicted in all of the retreating side azimuthal locations. Even though the coefficient of pressure is vastly different between the computation and experiment, the actual pressure difference may be less because the local dynamic pressure at 40% location on the retreating side is very low. The dynamic stall effect is seen in the upper surface pressures between ψ = 220–320 deg. The bumps in the surface pressures on the upper surface indicate the vortices that were also observed in the pressure contours at these azimuthal locations. The lower surface pressure indicates smooth attached flow in these azimuths as the blade is constantly increasing in pitch.

The prediction of the three-dimensional dynamic stall vortex formation and movement is believed to be a very challenging task using the present-day Navier–Stokes solvers. The present calculation does not adequately quantify the dynamic stall effects. This may be because of the coarseness of the grid and the algebraic turbulence model. It is hoped that with refined grid and two-equation turbulence models (like k-ε) this phenomena could be analyzed more quantitatively. Note that the computed pressures are the unsteady values obtained at that particular instant of time, whereas the experimental values are time averaged over several rotor revolutions.

Figure 9 shows the normal force coefficient time history at 77.5 and 92% radial locations, respectively. The inboard load predictions are underpredicted between ψ = 200–260 deg. The normal force coefficients in the outboard regions compare better with the experimental values.[15] The computed loads are plotted after each blade has traveled one full revolution. The experimental values are time averaged over several rotor revolutions. The dip in the force coefficient around an azimuth of 260 deg is believed to be because of the shedding of the dynamic stall vortex. In the tip region, beyond r/R = 0.87, the dynamic stall effect is not seen in the load plots. The negative and positive load regions around the azimuth are well predicted in the computations.

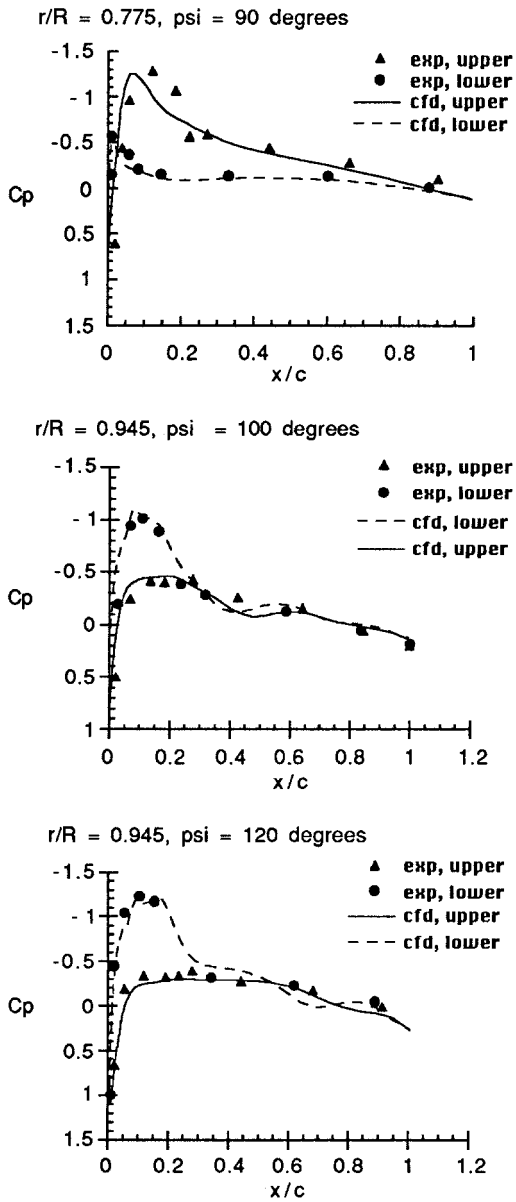

Fig. 7 Surface pressure distribution, second quadrant, M_{tip} = 0.628, advance ratio = 0.3, UH-60A baseline rotor.

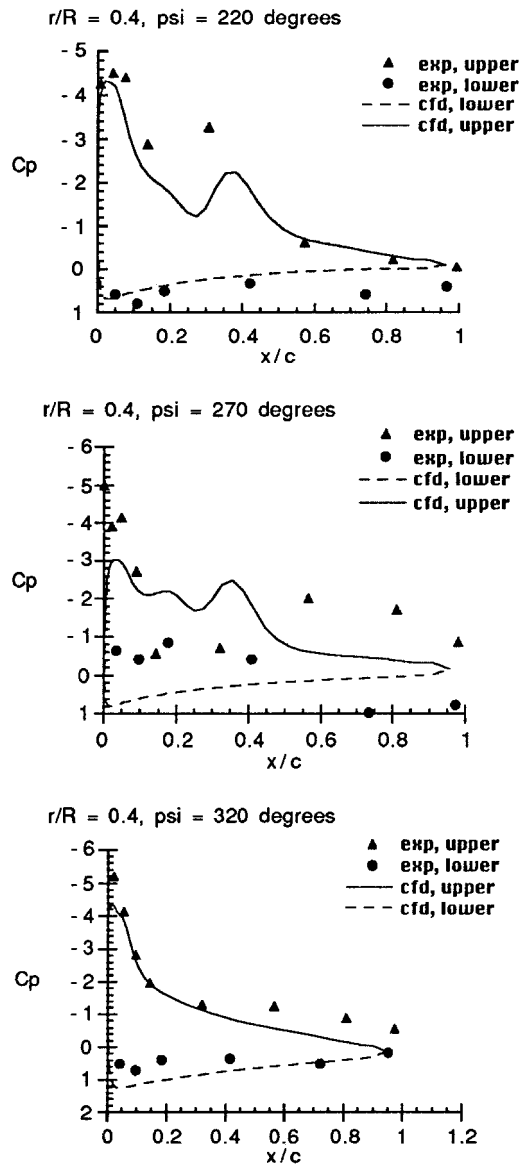

Fig. 8 Surface pressure distribution, retreating side, M_{tip} = 0.628, advance ratio = 0.3, UH-60A baseline rotor.

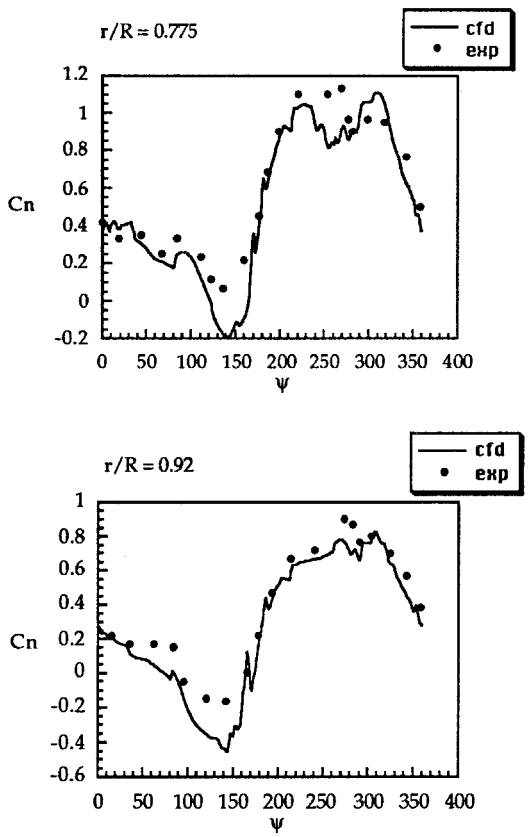

Fig. 9 Sectional normal force coefficient (nondimensionalized with local dynamic pressure) vs azimuth, UH-60A baseline rotor.

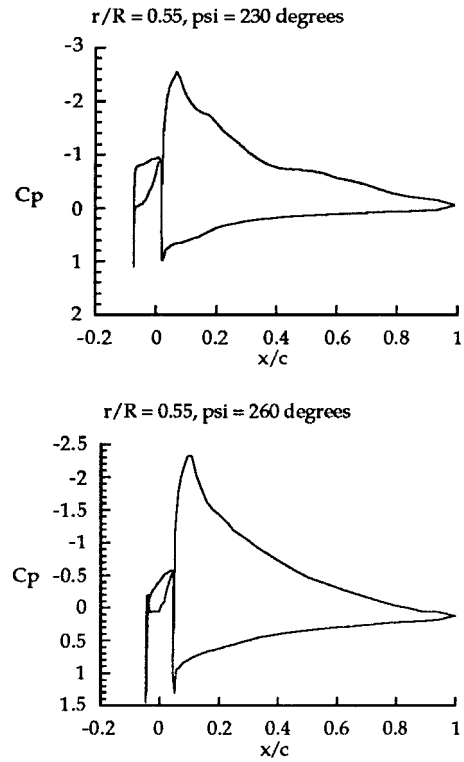

Fig. 10 Surface pressure distribution, 55% radial station, retreating side, M_{tip} = 0.628, advance ratio = 0.3, UH-60A slatted rotor.

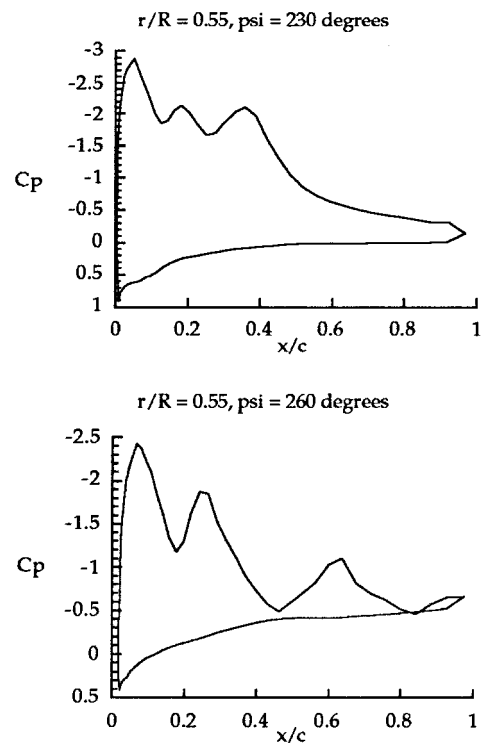

Fig. 11 Surface pressure distribution, 55% radial station, retreating side, M_{tip} = 0.628, advance ratio = 0.3, UH-60A baseline rotor.

UH-60A Slatted Rotor

The schematic of the UH-60A rotor blade with a partial span leading-edge slat is shown in Fig. 5. The slat spans up to 60% radius from the root of the blade. The location of the slat was chosen such that the slatted portion of the blade experienced high angle-of-attack subsonic flow. However, the analysis could be performed with the slat in any portion of the blade span using the present solver. The slat was not included near the tip region as it was not known a priori the transonic effects of the slat on the rotor performance.

The four-bladed H−O grid is used in the computation as shown in Fig. 2. This grid may not be the most efficient grid in capturing the rotor wake in forward flight because the grid is dense only near the tip region and is coarse away from the tip region. In forward flight, unlike the hover case, the rotor wake is convected aft of the rotor blade. With the present form of the grid, the tip vortices move away from the dense portions of the grid. A drawback of using the structured grids, as in the present case, is that it is very hard, if not impossible to adapt the grid locally. Unstructured grids may be very useful in these situations, where the grid adaption near the vortex regions becomes very easy. Such an unstructured grid approach is being pursued by Strawn and Barth.[18]

Figure 10 shows the surface pressures on the retreating side of the azimuth at ψ = 230 and 260 deg for the slatted rotor blade. Figure 11 shows the corresponding retreating blade surface pressures at 55% radial location for the baseline rotor. These azimuthal and radial locations are chosen to show that there is a reduction of dynamic stall because of the slat on the retreating side. For the baseline case, we start to observe the bumps on the upper surface pressure distribution, indicative of the dynamic stall vortex, at ψ = 230 deg. The corresponding pressure plot at ψ = 230 deg for the slatted rotor shows no bumps in the pressure distribution and indicates that there is no separation. The slat is shown to reduce the traditional massive separation, resulting in a smooth pressure distribution. By the time the blade reaches ψ = 290 deg, the flow recovers from the stall.

The sectional force coefficients of baseline and slatted rotors are plotted along the azimuth at 36 and 87% radial locations, as shown in Fig. 12. In the inboard regions (r/R = 0.55) the baseline C_n values show a sharp decrease, indicative of the

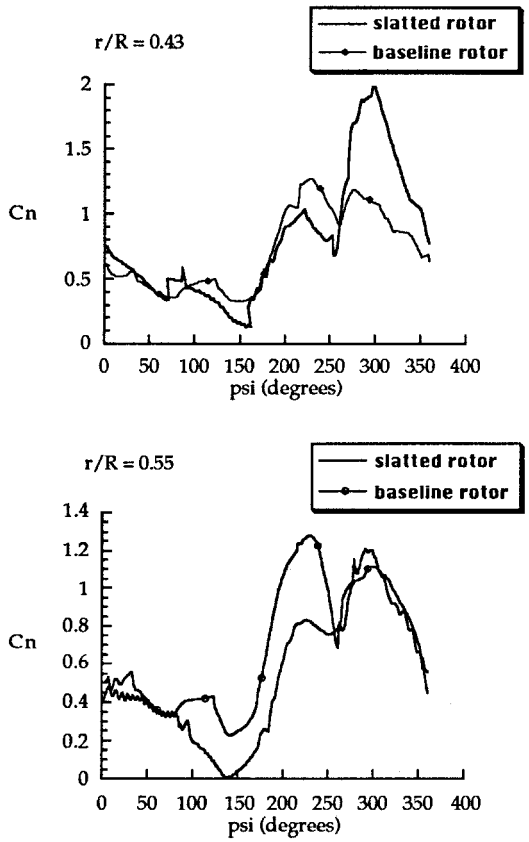

Fig. 12 Sectional normal force coefficient (nondimensionalized with local dynamic pressure) vs azimuth, UH-60A baseline and slatted rotors, $\mu = 0.3$.

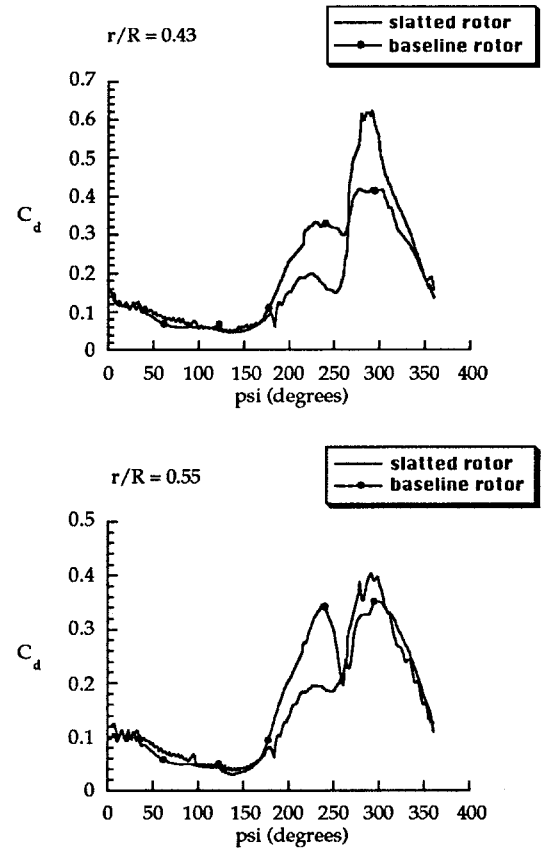

Fig. 13 Sectional drag coefficient (nondimensionalized with local dynamic pressure) vs azimuth, UH-60A baseline and slatted rotors, $\mu = 0.3$.

dynamic stall vortex shedding. The force coefficient in the slatted rotor case shows a smaller dip in the inboard regions near $\psi = 260$ deg. The decrease in C_n in the case of the slatted rotor around $\psi = 260$ deg is believed to be because of the change in local dynamic pressure in that azimuthal region and not because of the shedding of the dynamic stall vortex. This observation is based on the fact that no apparent separation was observed on the upper surface of the slatted blade on the retreating side of azimuth.

In the tip region of the blade where there is no slat, the force coefficients of the slatted and the baseline rotors are almost identical in their behavior along the azimuth. Another feature observed is that the slatted force coefficient in the second quadrant ($\psi = 90-180$ deg) is lower than the corresponding baseline values at some radial locations ($r/R = 0.43$ and 0.55). This is because the pitch distribution assumes a minimum in the second quadrant and the slat may be causing an additional download on the rotor blade. It should be noted that the pitch distribution is obtained from the trim condition of the baseline rotor. The trim condition obviously changes for the slatted rotor and should be calculated in an iterative process in future studies.

Figure 13 shows the variation of sectional drag coefficients of the baseline and slatted UH-60A rotors with the azimuth at different radial sections. The drag coefficients in the baseline and slatted rotor cases are almost identical on the advancing side (up to $\psi = 180$ deg) at 43 and 55% radial locations. A sharp dip is observed near $\psi = 250$ deg in the baseline rotor case. This phenomena was also observed in the sectional normal force coefficients (Fig. 12). This is because of the movement and shedding of the dynamic stall vortex. This sharp dip in the drag is not observed in the slatted rotor case and the drag values are lower compared to the baseline case. However, the drag values in the fourth quadrant ($\psi = 270-360$ deg) show that the slatted rotor causes a higher drag in the inboard

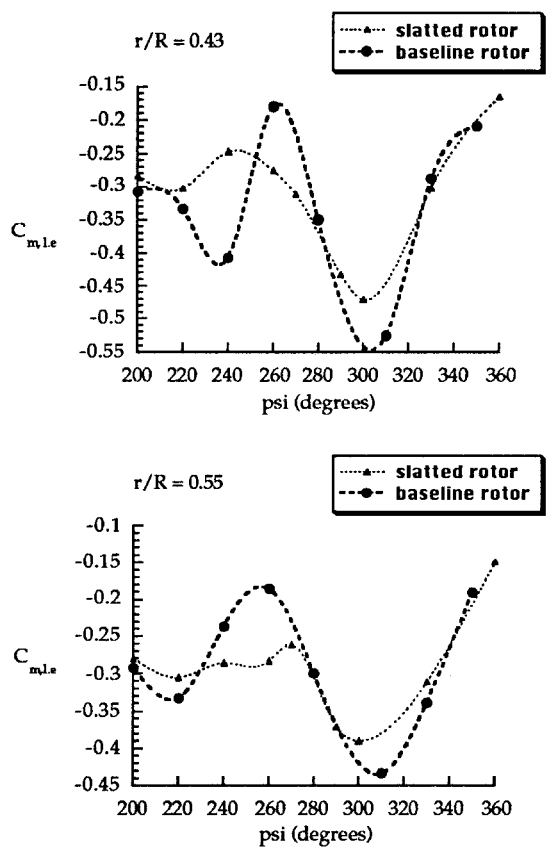

Fig. 14 Sectional moment coefficient (nondimensionalized with local dynamic pressure) on the retreating side, UH-60A baseline and slatted rotors.

regions than the baseline rotor. This additional drag is a lift-dependent drag caused by the slat, as seen in the sectional force coefficient plots (Fig. 12).

The sectional moment coefficient on the retreating side at different radial sections for the baseline and the slatted rotor cases are plotted in Fig. 14. The movement of the dynamic stall vortex in the baseline rotor case causes rapid changes in the pitching moment. In the slatted rotor case, there is no formation of the dynamic stall vortex and the corresponding pitching moment variation is not seen. The reduction of the pitching moment variation because of the slat is very beneficial in reducing the pitch link loads and the structural vibration levels.

Concluding Remarks

The present Navier–Stokes methodology is believed to be the first in its kind to be capable of analyzing unsteady three-dimensional viscous compressible flows over complex geometries that include rotor + slat/flap configurations undergoing arbitrary unsteady motion. The solver is capable of capturing rotor wakes from first principles without relying on external wake models. This wake-capturing capability is very useful in the analysis of rotor blades with complex shapes (e.g., slatted UH-60A rotor), where there is no wake experimental data available a priori.

The forward-flight analysis of the four-bladed UH-60A rotor with and without slat has been successfully performed using the present method. Pressure and load comparisons with experiments were done for the baseline UH-60A rotor. The leading-edge slat eliminated the retreating blade dynamic stall. The unsteady variations of the sectional loads and the pitching moments of the baseline rotor on the retreating side were not observed in the case of the slatted rotor. The slat appears very beneficial in the reduction of blade vibration levels and pitch link loads. In this particular forward-flight condition, the adverse effects on the advancing side because of the slat were not significant.

Acknowledgments

This work was supported by the U.S. Army Research Office under the Rotorcraft Center of Excellence (CERT) program. Thomas Doligalski was the Technical Monitor. The authors acknowledge the Pittsburgh Supercomputing Center and the Georgia Tech High Performance Computing Group for providing the computer resources.

References

[1]Dadone, L., "Helicopter Design DATCOM, Vol. I — Airfoils," NASA CR-153247, May 1976.

[2]Noonan, K. W., and Bingham, B. J., "Aerodynamic Characteristics of Three Helicopter Rotor Airfoil Sections from Model Scale to Full Scale at Mach Numbers from 0.35 to 0.9," NASA TP 1701, Army Aviation Research and Development Command, TR-80-B-5, Sept. 1980.

[3]McVeigh, M. A., and McHugh, F. J., "Recent Advances in Rotor Technology at Boeing Vertol," 38th Annual American Helicopter Society Forum, Anaheim, CA, May 1982.

[4]McAlister, K. W., Pucci, S. L., McCroskey, W. J., and Carr, L. W., "An Experimental Study of Dynamic Stall on Advanced Airfoil Sections, Volume 2: Pressure and Force Data," NASA TM 84245, Sept. 1982.

[5]Noonan, K. W., Allison, D. O., and Stanaway, S., "Investigation of Slotted Rotorcraft Airfoil at Mach Numbers Ranging from 0.2 to 0.88 at Full Scale Reynolds Numbers," American Helicopter Society Aeromechanics Specialists Conf., San Francisco, CA, Jan. 1994.

[6]Yu, Y., Lee, S., McAlister, K. W., and Tung, C., "High Lift Concepts for Rotorcraft Applications," 49th American Helicopter Society Annual Forum, St. Louis, MO, May 1993.

[7]Bangalore, A., and Sankar, L. N., "Numerical Analysis of Aerodynamic Performance of Rotors with Leading Edge Slats," *Computational Mechanics*, Vol. 17, No. 5, 1996, pp. 335–342; also AIAA Paper 95-1888, June 1995.

[8]Seddon, J., *Basic Helicopter Aerodynamics*, AIAA Education Series, AIAA, Washington, DC, 1990.

[9]Wake, B. E., and Sankar, L. N., "Solution of Navier-Stokes Equations for the Flow over a Rotor Blade," *Journal of the American Helicopter Society*, Vol. 34, No. 2, 1989, pp. 13–23.

[10]Roe, P. L., "Approximate Reimann Solvers, Parameter Vectors and Difference Schemes," *Journal of Computational Physics*, Vol. 43, 1981, pp. 357–372.

[11]Baldwin, B. S., and Lomax, H., "Thin Layer Approximation and Algebraic Model for Separated Turbulent Flow," AIAA Paper 78-0257, Jan. 1978.

[12]Bangalore, A., "Computational Fluid Dynamic Studies of High Lift Rotor Systems Using Distributed Computing," Ph.D. Dissertation, Georgia Inst. of Technology, Atlanta, GA, June 1995.

[13]Bangalore, A., Tseng, W., and Sankar, L. N., "A Multizone Navier-Stokes Analysis of Dynamic Lift Enhancement Concepts," AIAA Paper 94-0164, Jan. 1994.

[14]Sankar, L. N., Phaengsook, N., and Bangalore, A., "Effects of Icing on the Aerodynamic Performance of High Lift Airfoils," AIAA Paper 93-0026, Jan. 1993.

[15]Lorber, P. F., "Aerodynamic Results of a Pressure Instrumented Model Rotor Test at the DNW," *Journal of the American Helicopter Society*, Vol. 36, No. 4, 1991, pp. 66–76.

[16]Ahmad, J. U., and Duque, E. P. N., "Helicopter Rotor Blade Computation in Unsteady Flows Using Moving Overset Grids," *Journal of Aircraft*, Vol. 33, No. 1, 1996, pp. 54–60.

[17]Ahmad, J. U., Bauchau, O. A., and Duque, E. P. N., "Multidisciplinary Application of Advanced CFD Method to Elastic Helicopter Blades," 6th International Symposium on CFD, Lake Tahoe, CA, Sept. 1995.

[18]Strawn, R. J., and Barth, J. T., "A Finite-Volume Euler Solver for Computing Rotary-Wing Aerodynamics on Unstructured Meshes," *Journal of the American Helicopter Society*, Vol. 38, No. 2, 1993, pp. 61–67.